Journal of Magnetism and Magnetic Materials 443 (2017) 45–50

Contents lists available at ScienceDirect

Journal of Magnetism and Magnetic Materials

journal homepage: www.elsevier.com/locate/jmmm

Research articles

Experimental and theoretical investigation of Bixbyite $(Mn_{0.8}Ni_{0.2})_2O_3$ nanoparticles for magnetic and electrochemical applications

S. Ramesh [a,c,*], Potu Venugopal [b], Edgar Mosquera [d]

[a] Laboratorio de Materiales Funcionales a Nanoescala, Departamento de Ciencia de los Materiales, Universidad de Chile, Beauchef 851, Santiago, Chile
[b] Department of Chemistry, School of Physical, Chemical and Applied Sciences, Pondicherry University, Pondicherry 605014, India
[c] Department of Chemistry, Saveetha School of Engineering, Saveetha University, Chennai 602105, India
[d] Departamento de Física, Universidad del Valle, A.A. 25360 Cali, Colombia

ARTICLE INFO

Article history:
Received 10 November 2016
Received in revised form 21 May 2017
Accepted 12 July 2017
Available online 13 July 2017

Keywords:
Sol-gel
X-ray diffraction
High-resolution electron microscopy
Nanocrystalline materials
Magnetic materials

ABSTRACT

Synthesis of Bixbyite phase nanocrystalline $(Mn_{0.8}Ni_{0.2})_2O_3$ is achieved by a sol–gel method. X-ray diffraction pattern of the sample reveals the formation of cubic lattice type nanocrystalline with Ia-3 space group. The high-resolution transmission electron microscopy images show irregularly shaped cubic nanoparticles with average crystallite size of 25 nm. Symmetric anodic and cathodic cyclic Voltammetry curve suggests that the nanoparticles are favorable to fast redox reactions. The hysteresis behavior of the magnetization curve shows the ferromagnetic nature of the sample. Band structure and spin-polarized partial density of states confirm the half-metallic and ferromagnetic behavior of the sample.

1. Introduction

Multifunctional nanostructured materials which comprise several properties are attracted great attention due to their applications in the areas such as photocatalysts [1–3], electrocatalysts [4,5], spintronics [6–8], optoelectronics [9], magnetic and electronic devices [10,11]. Manganese oxide nanoparticles have been extensively studied as most promising materials for energy applications due to their advantages like flexible and controllable physicochemical properties through size and shape [3]. The several manganese oxides, includes MnO_2, Mn_2O_3, Mn_3O_4, and Mn_5O_8 are attractive towards electro and photocatalysis, sensors, secondary batteries and supercapacitors [2–6]. In particular, Mn_2O_3 nanomaterials have gained more attention for their several applications in the fields of catalysis, magnetism, energy storage and conversion [12,13]. The physiochemical properties of Mn_2O_3 nanostructures can be tailored by alternating the composition, structure, morphology and synthesis methods. Recently the efficiency of the manganese oxides catalytic activities particularly in the oxidation reduction reaction is found to be in the order of $Mn_5O_8 < Mn_3O_4 < Mn_2O_3$. Several reports on manganese oxides with different morphologies like the plate, flower, and clusters for various applications are achieved by careful choice of ions such as Al, Cr, Fe, Co, Cu, In, La, Li, Mg, Ni, Tm and Zn [14]. Nickel oxides are also an interesting and promising candidate for the magnetic, electronic, catalytic and electrochemical application. Nickel integrated manganese oxides are reported as pseudocapacitive with large specific capacitance and greater electrochemical activity but still limited [15–17]. The greater efficiency was achieved with NiMnO than Mn, α-MnO2, and Mn_2O_3. Furthermore, the ferromagnetic behavior enabled due to Ni incorporation which are advantageous, to recover from the solution after the reaction using a magnet. Also, Bixbyite phase metal oxides exist over a limited range of compositions hence in this report we studied the multifunction properties of $(Mn_{0.8}Ni_{0.2})_2O_3$ composition [18–21]. In this perspective, we intend to prepare the multifunctional Bixbyite phase $(Mn_{0.8}Ni_{0.2})_2O_3$ nanomaterial.

Recently, several wet chemical methods have been used to synthesis multifunctional materials. The methods like hydrothermal, co-precipitation, sol-gel, combustion and spray pyrolysis are mostly used [2]. Among all them, sol-gel synthesis is an effective method to produce multifunctional materials due to low-processing cost, energy efficiency, and easy to produce homogeneous powder at multiscale [22–24]. Therefore, in this present work, we opted for the sol-gel approach to the synthesis of

* Corresponding author at: Laboratorio de Materiales Funcionales a Nanoescala, Departamento de Ciencia de los Materiales, Universidad de Chile, Beauchef 851, Santiago, Chile.
E-mail address: rameshsiva_chem@yahoo.com (S. Ramesh).

http://dx.doi.org/10.1016/j.jmmm.2017.07.043
0304-8853/

nanocrystalline $(Mn_{0.8}Ni_{0.2})_2O_3$ heterobimetallic nickel-manganese oxides and studied the structural, morphological, electrochemical, electronic and magnetic properties.

2. Experimental

2.1. Synthesis of $(Mn_{0.8}Ni_{0.2})_2O_3$ nanoparticles

The sol-gel process was adopted to synthesize the nanocrystalline $(Mn_{0.8}Ni_{0.2})_2O_3$ materials. Reagents are used as purchased, without further purification. The calculated weight of nickel and manganese nitrate solutions were mixed and stirred for 30 min. Later, 50 ml of 2 M nitric acid is added and the pH of the solution is maintained at 5 using liquid ammonia. The resulting mixture is continuously stirred at 333 K until it turns to be a transparent gel. Further, the gel network was broken at 373 K for 1 h. Finally, the sample is sintered at 773 K for 5 h to achieve homogeneous sample. The systematic preparation of the nanoparticles is shown in the supplementary information (Fig. S1).

2.2. Characterizations

The phase identification and structural information of the sample were determined using powder X-ray diffraction (PXRD; PANalytical X'Pert PRO diffractometer with monochromatic $Cu_{K\alpha}$ as a source at 40 kV/30 mA). A scanning electron microscopy (SEM; Hitchi-S3000H) with energy dispersive X-ray spectroscopy (EDX) was used to observe the morphology of the synthesized powder. Structural information was acquired by high-resolution transmission electron microscopy (HR-TEM) images, selected area electron diffraction (SAED) patterns, and X-ray (EDX) mapping using a JEOL 2000 FX-II, operated at 200 kV. TEM sample was prepared and dispersed in a dilute medium and few drops of the suspension were dropped and evaporated onto a carbon-coated nickel grid. The electrochemical properties of the sample were observed using cyclic Voltammetry (CV) in a three electrode system. For CV measurements, the electrode of reference and counter electrode used were KCl-saturated Ag/AgCl and Pt wire, respectively. The working electrode fabricated using $(Mn_{0.8}Ni_{0.2})_2O_3$ and carbon powders were mixed with polyvinylidene fluoride (PVDF) in the weight ratio of 85:5:5 to ensure sufficient electronic conductivity. The electrolyte comprised a 1 M aqueous KOH solution. Magnetic properties were studied by a vibrating sample magnetometer (VSM; LAKESHORE VSM 7404).

2.3. Computational details

First principle calculation is based on the density functional theory (DFT), which is used for geometry optimization and electronic property calculations by Accelrys package. Generalized gradient approximation (GGA) was implemented in the calculations. The geometry optimization, band structure, and density of states (DOS) were achieved using periodic boundary conditions, and Brillouin zone integration with 2x2x2 Monkhorst-Pack (MP). The residual force condition for convergence is set to be 0.01 eV/Å [25].

3. Results and discussions

3.1. X-ray diffraction

Fig. 1 shows the room temperature powder XRD patterns of $(Mn_{0.8}Ni_{0.2})_2O_3$ nanoparticles. All the peaks in the diffraction pattern of $(Mn_{0.8}Ni_{0.2})_2O_3$ were indexed to single-phase cubic lattice type with Ia-3 (206) space group. The PXRD pattern was fitted for the refinement using the pseudo-Voigt function with polynomial background subtraction. Structural refinement of the sample was achieved by Rietveld refinement analysis using FullProf package profile is shown in the supplementary information (Fig. S2). The obtained unit cell parameters *a*, calculated density *d*, and cell volume *V* of the cubic crystal system are 10.8167 Å, 3.31 g/cm^3, 1265.56 Å^3, respectively. The average crystallite size was calculated using the full width at half maximum (FWHM) of all the peaks by the Debye-Scherrer formula, which is shown in Eq. (1) [26].

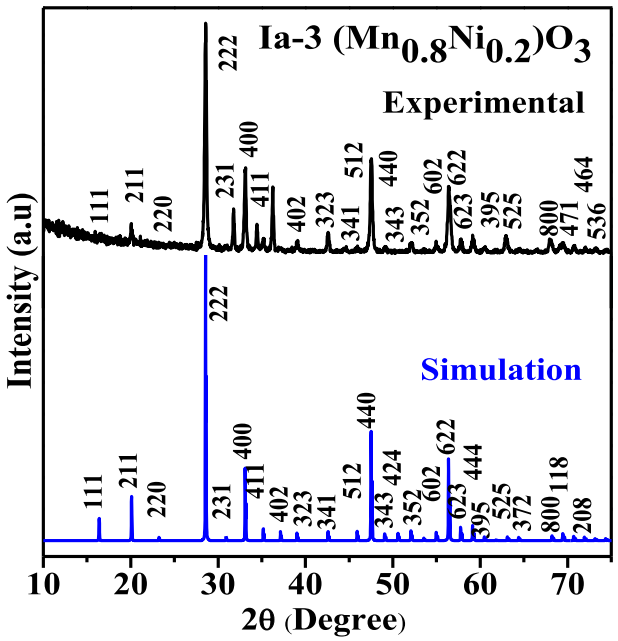

Fig. 1. Powder X-ray Diffraction patterns of $(Mn_{0.8}Ni_{0.2})_2O_3$ nanoparticles.

$$D = \frac{K\lambda}{\beta_{1/2}cos\theta} \quad (1)$$

where D is crystallite size, K is Scherrer constant, λ is the wavelength of $Cu_{K\alpha}$ radiation, β stands for half-width of the diffraction peak, and θ is the Bragg angle of the X-ray diffraction. The estimated average crystallite size of the nanocrystalline $(Mn_{0.8}Ni_{0.2})_2O_3$ is 25 nm.

The indexed X-ray refinement suggested a primitive cubic crystal system with the Ia-3 space group. The refinement was converged and lattice parameters were compatible with $(Mn_{0.5}Fe_{0.5})_2O_3$ (cI80, 206) structure type. The crystal structure of $(Mn_{0.8}Ni_{0.2})_2O_3$ is shown in Fig. 2(a). In the crystal structure, manganese and nickel atoms are shared in the Wyckoff position of 8b (0.25, 0.25, 0.25), 24d (0.9722, 0, 0.25) and oxygen atoms at 48e (0.25, 0.25, 0.25). The cations in the 8b positions are in octahedral geometry by six oxygen ions at three different distances (2.154, 2.287 and 2.143). The cations at 24d positions are in tetrahedral geometry bonded with oxygen by two different bond lengths. The selected bond lengths in the asymmetric unit, Mn1/Ni3-O2, Mn4/Ni5-O2 are 2.2364 and 2.2940 Å, respectively.

The compositions of the compound achieved from the structural refinement of XRD pattern is supported with elemental analysis by EDX data. The atomic coordinates and selective bond lengths are listed in supporting information (Tables S1, S2). Fig. 2 (b) shows the complete charge distribution mapping of the sample along the *c*-axis. The high electron distribution suggests that the interfaces are mostly metallic nature. The radius of the circle at 8b position shows ionic character, also some partial localization in the region between the two cations at 24d positions is a partial

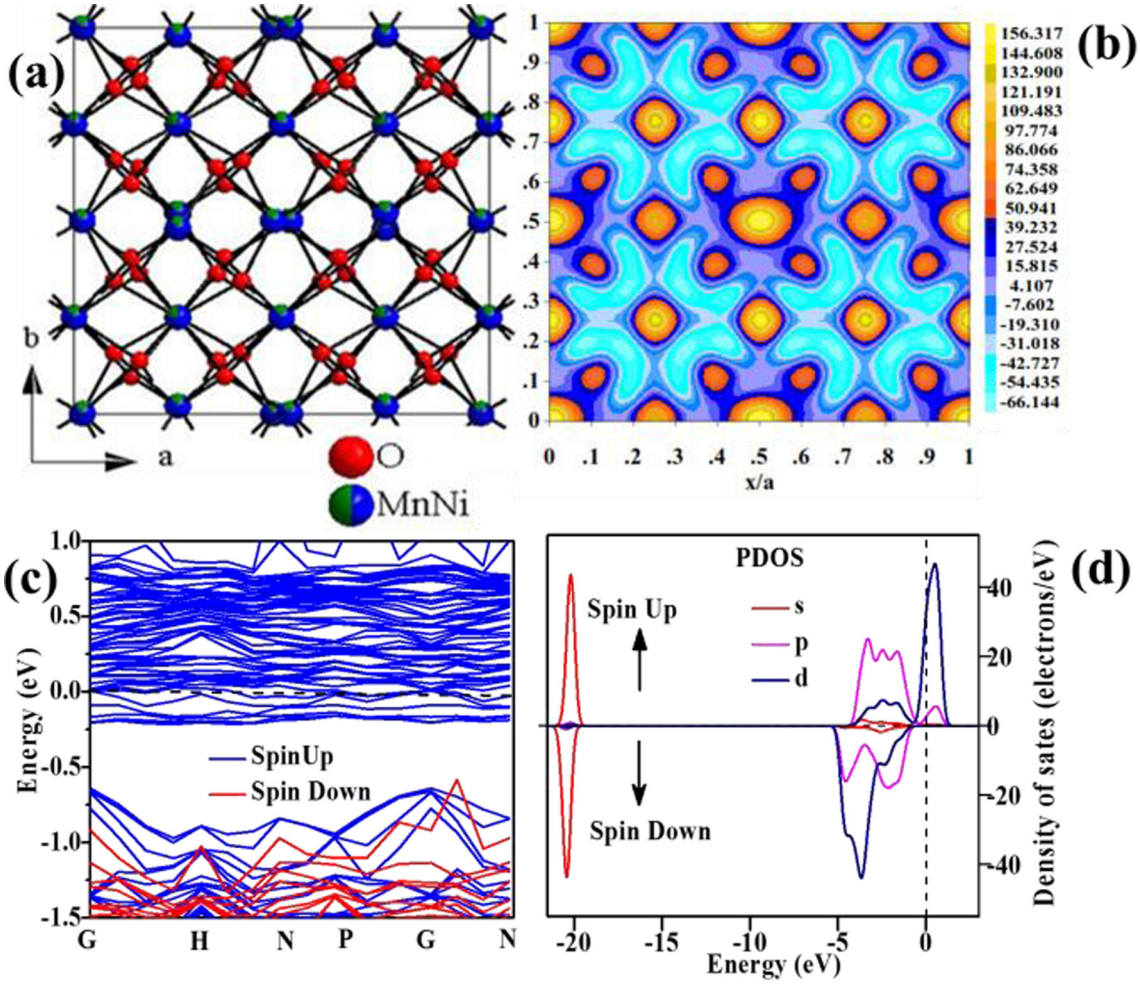

Fig. 2. (a) Crystal structure, (b) electron distribution map, (c) band structure and, (d) partial density of states of $(Mn_{0.8}Ni_{0.2})_2O_3$ nanoparticle.

covalent character of the Ni/Mn-O bond. The asymmetrical counter shapes around the Ni/Mn and O ions in the *xy*-plane (0 0 1) show the combination of covalent and ionic characters in $(Mn_{0.8}Ni_{0.2})_2O_3$.

3.2. Electronic structure

To visualize the electronic behavior, band structure and density of states (DOS) we performed DFT calculation. In the band structure (Fig. 2(c)), the valence band maximum and conductance band minimum are crossing at the Fermi level which suggests that the sample is metallic. Further, to understand the electronic behavior of the sample, we execute the spin-polarized calculation shown in the supplementary information (Fig. S5). The up-spins in the electronic band structure is distributed both above and below the Fermi level, whereas the down-spins are only below the Fermi level, which suggests the ferromagnetic interaction between the atoms and half-metallic behavior in the sample [27]. The spin polarized DOS (Fig. 2(d) and supporting information, Fig. S5) shows the strong hybridization found in the Mn/Ni-3d states with O-2p states. The down-spins at below Fermi level and up-spins above the Fermi level of $Mn_{0.81}Ni_{0.19}$ (8b) is more dominating than $Mn_{0.76}Ni_{0.24}$ (24d) and O (48e). The up-spins of O (48e) shows more dominant below at the Fermi level. Thus, the mismatch of up-spins and down-spins confirms the half-metallicity and ferromagnetism of the sample. The ferromagnetic behavior of the sample arises from the *d*-states of Mn/Ni atoms of Mn/Ni-3d at 24d atomic position.

3.3. Electron microscopy

The scanning electron microscopy (SEM) and transmission electron microscopy (TEM) images were used to examine the morphology of $(Mn_{0.8}Ni_{0.2})_2O_3$ nanoparticles. The nanocrystalline and porous nature of the sample is confirmed by SEM images at different magnifications (supplementary information, Fig. S5). Fig. 3(a) show the TEM images of the samples, which exhibit irregularly shaped cubic nanoparticles with size around 25–60 nm. The particles are slightly elongated and a few are aggregated. Further insight into the structural information of the nanocrystalline $(Mn_{0.8}Ni_{0.2})_2O_3$, we have performed high-resolution TEM (HRTEM) imaging of a randomly selected area. A clear lattice fringe of the sample is shown in Fig. 3(b). HRTEM images of individual particles (Fig. 3(b)) show *d* spacing of 0.27, 0.31 and 0.44 nm and corresponds to (0 0 4), (2 2 2) and (1 1 2) lattice planes of the Ia-3 structure. This preferential growth is consistent with XRD analysis (Fig. 3(c)), which shows an intensive diffraction peak being indexed to the (2 2 2) planes. The elemental distribution and homogeneity of the sample are confirmed using X-ray mapping. The mapping suggests the presence of Mn, Ni, and O in the frames and it is distributed uniformly throughout the sample surfaces. The amounts of Mn and O are higher than that of Ni as expected (Fig. 3(a)).

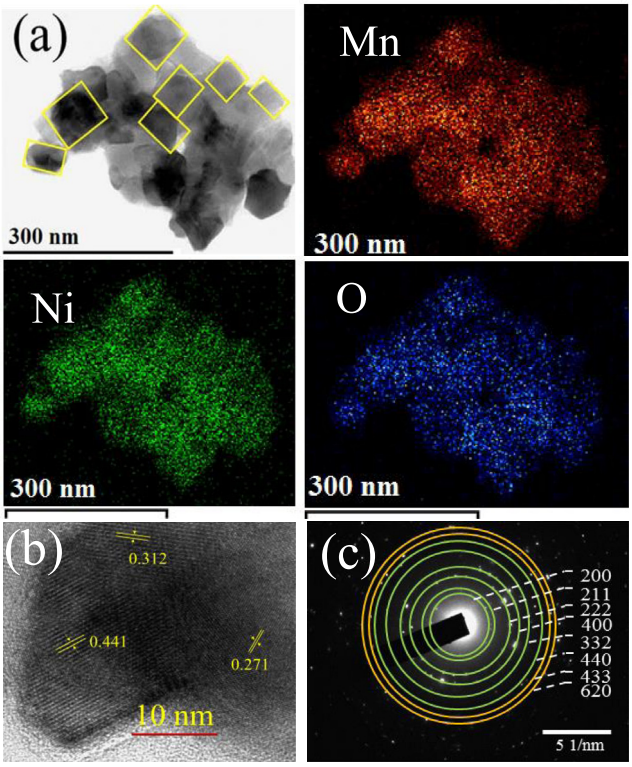

Fig. 3. (a) TEM image and elemental mapping, (b) HRTEM image, and (c) SAED pattern of $(Mn_{0.8}Ni_{0.2})_2O_3$ nanoparticles.

3.4. Electrochemical studies

The electrochemical property of the sample was characterized by cyclic Voltammetry (CV) measurements. The CV curves of $(Mn_{0.8}Ni_{0.2})_2O_3$ electrode was recorded in the potential range from 0 V to 0.35 V at the different scanning rate in 1 M KOH electrolyte are shown in Fig. 4(a). Distinct anodic and cathodic peaks around 0.1 V and 0.3 mV are attributed to the reversible conversion between Mn/Ni^{2+} to Mn/Ni^0 [28–30]. During the time of increasing the scan rate the current density also increases with similar shape and nature of the curves. The increase in the current density suggests that the nanoparticles are favorable to fast redox reactions [31–33]. At higher scan rate the CV curves produce noticeable symmetry with cathodic and anodic potentials are shifted to more positive and negative range. The increase of anodic and cathodic potentials are attributed to either resistance in electron hopping or restraint the ion diffusion rate to electronic neutralization while the redox reaction [34]. The symmetric nature of the redox peaks inferring a great reversibility of $(Mn_{0.8}Ni_{0.2})_2O_3$ nanoparticles. The specific capacitance (Cs, F g^{-1}) of the current sample is determined by integrating the area under the CV curves using the relation given below (Eq. (2)) [35],

$$Cs = \frac{1}{v\omega(\Delta V)} \int_{V_a}^{V_c} i(V)dV \tag{2}$$

where ΔV – applied potential limit (V_a to V_c), v (mV s^{-1}) – scan rate, and ω (g) – the weight of the current sample. Fig. 4(b) shows the specific capacitance of $(Mn_{0.8}Ni_{0.2})_2O_3$ electrodes is 80 Fg^{-1}.

3.5. Magnetic studies

Fig. 4(c) illustrates the magnetization curve of synthesized $(Mn_{0.8}Ni_{0.2})_2O_3$ nanoparticles was recorded in the range of ±12,000 G at 300 K. Several reports on magnetic behavior of undoped Mn_2O_3 exhibits as paramagnetic and antiferromagnetic behavior [36,37]. However, the hysteresis behavior of the $(Mn_{0.8}Ni_{0.2})_2O_3$ magnetization curve indicates that the nanoparticles show ferromagnetic behavior. The Ni incorporated

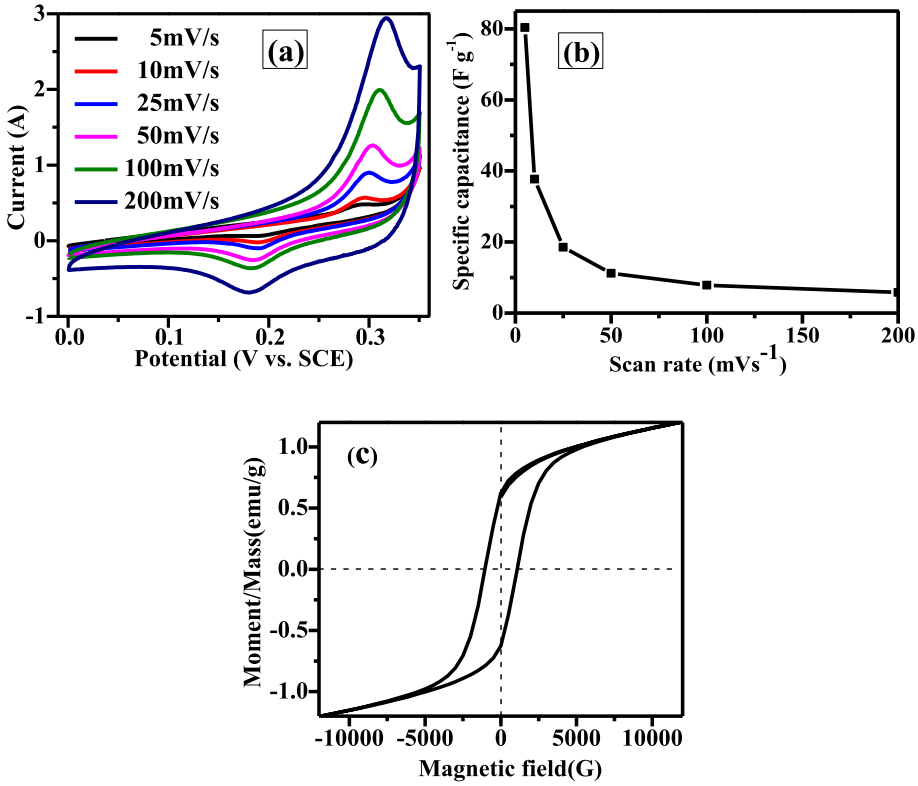

Fig. 4. (a) Cyclic voltammetry at different scanning rates (b) specific capacitance (c) magnetization plot of $(Mn_{0.8}Ni_{0.2})_2O_3$ nanoparticles.

Mn_2O_3 create chemically two different Mn ions at 8b and 24d Wyckoff position which forms Mn^{3+} and Mn^{4+} ions. Hence multiple exchange interactions are expected, (i) antiferromagnetic super exchange $Mn^{3+}-O_v-Mn^{3+}$ (ii) $Mn^{4+}-O_v-Mn^{4+}$ and ferromagnetic double exchange interactions $Mn^{3+}-O_v-Mn^{4+}$ in the sample [37]. In this sample the ferromagnetic double interactions are dominating than other two antiferromagnetic super exchange interaction. In addition, oxide nanoparticles may exist substantial amount of oxygen vacancies especially on the surface. Coey et al. predicted that the oxygen vacancy form F centers with tapped electrons are overlap with metal d (Mn-O_v-Mn) orbital leads to ferromagnetic nature [38–41]. Thus, the ferromagnetic behavior of this sample is principally originated from the combination of double exchange interaction between the $Mn^{3+}-O_v-Mn^{4+}$ ions and presence of oxygen vacancy. Magnetic susceptibility, (χ) of the sample was calculated according to the relation below (Eq. (3)) [2],

$$M = \frac{\chi}{H} \tag{3}$$

where M – magnetization (emu/g) and H – applied magnetic field. The magnetic susceptibility value of the sample is 2.70×10^{-1} (emu/gG). Saturation magnetization (Ms), remanence (Mr), coercivity (Hc), squareness ratio (SQR) and switching field distribution (SFD) are extracted from the hysteresis curve. The high value of Ms (1.199 emu/g) and Mr (0.59 emu/g) of the sample confirms the presence of multi-domains in the sample. The Hc (1134 G) and χ (3.85×10^{-1} emu/gG) indicates that the sample belongs to the category of hard magnetic materials. The SQR and SFD are an important to characterize the magnetic properties of magnetic media. The squareness ratio (SQR) is estimated using the ratio of (Mr/Ms) [42] and SFD is estimated from $\Delta H/Hc$, where ΔH – full width at half maximum of the differentiated curve dM/dH [43–45]. The SFD provides the information of magnetization reversal of magnetic materials. The reported SFD and SQR of γFe_2O_3 and $Fe_{1-x}M_xO_3$ (M-Ni, CO, Ba, Mn, Nb and Si) are in the range of 0.28–0.60 and 0.2–1.9 respectively [46–50]. The High Hc and small SFD are required for high-density recording media [51]. The estimated value of SFD and SQR values of $(Mn_{0.8}Ni_{0.2})_2O_3$ are 3.18 and 0.29 respectively which was narrower than doped and undoped ferrite and other oxides. The significant value of SQR and SFD suggests that the sample can be used as magnetic storage applications. The smooth hysteresis curve without jerks also confirms homogeneity of the sample.

4. Conclusion

In summary, a cubic lattice Ia-3 space group multifunctional nanoparticles of $(Mn_{0.8}Ni_{0.2})_2O_3$ were successfully synthesized by sol-gel technique. The cyclic Voltammetry curves confirm the reversible redox process involves in the system. The shape of the hysteresis and other magnetic parameters reveals that the sample is ferromagnetic at room temperature. The band structure and partial DOS are confirmed the half-metallic and ferromagnetic nature of the sample.

Acknowledgments

The author SR thanks to the Department of Material Science, Faculty of Mathematical and Physical Sciences, University of Chile. Santiago, Chile and the CONICYT – Chile, Project N°. 3170052.

Appendix A. Supplementary data

Figures: Flow chart of the synthesis, Band structure with the partial density of states. SEM images, EDX profile and x-ray mapping, Table: Atomic parameters of $(Mn_{0.8}Ni_{0.2})_2O_3$ nanoparticles. Supplementary data associated with this article can be found, in the online version, at http://dx.doi.org/10.1016/j.jmmm.2017.07.043.

References

[1] M. Gowrishankar, D.R. Babu, S. Madeswaran, J. Magn. Magn. Mater. 418 (2016) 54–61.
[2] S. Ramesh, J.V. Ramaclus, E. Mosquera, B.B. Das, RSC Adv. 6 (2016) 6336–6341.
[3] W. Wei, X. Cui, W. Chen, D.G. Ivey, Chem. Soc. Rev. 40 (2011) 1697–1721.
[4] C.H. Choi, S.H. Park, S.I. Woo, Phys. Chem. Chem. Phys. 14 (2012) 6842–6848.
[5] A. Ganguly, O. Anjaneyulu, K. Ojha, A.K. Ganguli, CrystEngComm 17 (2015) 8978–9001.
[6] K. Jayanthi, M. Rajan Mohan Rao, L. Satyanarayana, M. Manivel Raja, K. Mohan Kumar, V.V.S.S. Srikanth, M. Subramanian, C. Anandan, S.V. Manorama, RSC Adv. 6 (2016) 29869–29879.
[7] S.A. Ahmed, S.H. Mohamed, J. Magn. Magn. Mater. 324 (2012) 812–817.
[8] R.A.P. Ribeiro, A. Camilo Jr., S.R. de Lazaro, J. Magn. Magn. Mater. 394 (2015) 463–469.
[9] T. Lantri, S. Bentata, B. Bouadjemi, W. Benstaali, B. Bouhafs, A. Abbad, A. Zitouni, J. Magn. Magn. Mater. 419 (2016) 74–83.
[10] N. Ortega, K. Ashok, J.F. Scott, S.K. Ram, J. Phys.: Condens. Matter 27 (2015) 504002.
[11] N. Ghosh, S. Datta, B. Ghosh, J. Magn. Magn. Mater. 382 (2015) 277–282.
[12] P.F. Smith, B.J. Deibert, S. Kaushik, G. Gardner, S. Hwang, H. Wang, J.F. Al-Sharab, E. Garfunkel, L. Fabris, J. Li, G.C. Dismukes, ACS Catal. 6 (2016) 2089–2099.
[13] S. Maiti, A. Pramanik, S. Mahanty, CrystEngComm 18 (2016) 450–461.
[14] M.F. Bekheet, I. Svoboda, N. Liu, L. Bayarjargal, E. Irran, C. Dietz, R.W. Stark, R. Riedel, A. Gurlo, J. Solid State Chem. 241 (2016) 54–63.
[15] H. Sim, C. Jo, T. Yu, E. Lim, S. Yoon, J.H. Lee, J. Yoo, J. Lee, B. Lim, Chem. A Eur. J. 20 (2014) 14880–14884.
[16] T. Nguyen, M. Boudard, L. Rapenne, M.J. Carmezim, M.F. Montemor, J. Mater. Chem. A 3 (2015) 10875–10882.
[17] M. Li, J.P. Cheng, J. Wang, F. Liu, X.B. Zhang, Electrochim. Acta 206 (2016) 108–115.
[18] N. Reeves-McLaren, J. Sharp, H. Beltrán-Mir, W.M. Rainforth, A.R. West, Proc. Math. Phys. Eng. Sci. R. Soc. 472 (2016) 20140991.
[19] C. Sena, M.S. Costa, E.L. Muñoz, G.A. Cabrera-Pasca, L.F.D. Pereira, J. Mestnik-Filho, A.W. Carbonari, J.A.H. Coaquira, J. Magn. Magn. Mater. 387 (2015) 165–178.
[20] L. Arda, M. Acikgoz, Y. Aktas, O. Cakiroglu, N. Dogan, J. Magn. Magn. Mater. 373 (2015) 65–67.
[21] S.K.S. Patel, P. Dhak, M.-K. Kim, J.-H. Lee, M. Kim, S.-K. Kim, J. Magn. Magn. Mater. 403 (2016) 155–160.
[22] L. Sun, R. Zhang, Z. Wang, L. Ju, E. Cao, Y. Zhang, J. Magn. Magn. Mater. 421 (2017) 65–70.
[23] B.B. Das, S. Ramesh, AIP Conf. Proc. 1003 (2008) 85–87.
[24] O. Opuchovic, A. Kareiva, K. Mazeika, D. Baltrunas, J. Magn. Magn. Mater. 442 (2017) 425–433.
[25] S. Ramesh, S. Marutheeswaran, J.V. Ramaclus, D.C. Paul, Superlattices Microstruct. 76 (2014) 213–220.
[26] S. Ramesh, B.B. Das, J. Korean Chem. Soc. 55 (2011) 502–508.
[27] Y. Zhou, H. Lu, X. Zu, F. Gao, Sci. Rep. 6 (2016) 19407.
[28] B. Liu, X. Hu, H. Xu, W. Luo, Y. Sun, Y. Huang, Sci. Rep. 4 (2014) 4229.
[29] C. Zhang, J.-G. Wang, D. Jin, K. Xie, B. Wei, Electrochim. Acta 180 (2015) 990–997.
[30] J.-G. Wang, C. Zhang, D. Jin, K. Xie, B. Wei, J. Mater. Chem. A 3 (2015) 13699–13705.
[31] Y. Xu, J. Wei, L. Tan, J. Yu, Y. Chen, J. Mater. Chem. A 3 (2015) 7121–7131.
[32] L. Xuan, L. Chen, Q. Yang, W. Chen, X. Hou, Y. Jiang, Q. Zhang, Y. Yuan, J. Mater. Chem. A 3 (2015) 17525–17533.
[33] Y. Zhu, C. Cao, S. Tao, W. Chu, Z. Wu, Y. Li, Sci. Rep. 4 (2014) 5787.
[34] Y. Zhu, C. Cao, RSC Adv. 5 (2015) 83757–83763.
[35] Z. Wu, X.-L. Huang, Z.-L. Wang, J.-J. Xu, H.-G. Wang, X.-B. Zhang, Sci. Rep. 4 (2014) 3669.
[36] L.M.E. Nadi, Modern Trends in Physics Research, Third International Conference on Modern Trends in Physics Research, MTPR-08, Cairo, Egypt, 6–10 April 2008 (2011).
[37] K.S. Pugazhvadivu, K. Ramachandran, K. Tamilarasan, Phys. Proc. 49 (2013) 205–216.
[38] D.Y. Guo, Z.P. Wu, Y.H. An, X.C. Guo, X.L. Chu, C.L. Sun, L.H. Li, P.G. Li, W.H. Tang, Appl. Phys. Lett. 105 (2014) 023507.
[39] Y. An, S. Wang, D. Feng, Z. Wu, J. Liu, Appl. Surf. Sci. 276 (2013) 535–538.
[40] S. Ghosh, G.G. Khan, K. Mandal, ACS Appl. Mater. Interfaces 4 (2012) 2048–2056.
[41] A. Sundaresan, R. Bhargavi, N. Rangarajan, U. Siddesh, C.N.R. Rao, Phys. Rev. B 74 (2006) 161306.
[42] M.N. Akhtar, M.A. Khan, M. Ahmad, M.S. Nazir, M. Imran, A. Ali, A. Sattar, G. Murtaza, J. Magn. Magn. Mater. 421 (2017) 260–268.
[43] S. Kawahara, Y. Nakano, Y. Shimizu, Y. Yamauchi, Google Patents, 1993.
[44] V. Harikrishnan, R. Ezhil Vizhi, J. Magn. Magn. Mater. 418 (2016) 217–223.

[45] H.Z. Yang, Y.J. Chen, S.H. Leong, C.W. An, K.D. Ye, J.F. Hu, J. Magn. Magn. Mater. 423 (2017) 27–33.
[46] I.O. Troyanchuk, A.A. Shemyakov, V.K. Prokopenko, Phys. Status Solidi (A) 113 (1989) K107–K109.
[47] A. Sebt, M. Akhavan, J. Magn. Magn. Mater. 237 (2001) 111–118.
[48] G. Bate, J. Magn. Magn. Mater. 100 (1991) 413–424.
[49] I. Honma, M. Hirai, M. Amano, N. Takumi, Google Patents, 1986.
[50] Y.K. Hong, H.S. Jung, P.R. Taylor, Google Patents, 2001.
[51] F.C. Gaspare Varvaro, Ultra-High-Density Magnetic Recording: Storage Materials and Media Designs, CRC Press, Taylor & Francis Group, 2016.